HOKKAIDO UNIVERSITY

Title	Elucidation of electrochemical and morphological difference of carbon steel corroded in aqueous chloride solutions at low temperatures
Author(s)	Shen, Tong; Sakairi, Masatoshi
Citation	Electrochimica acta, 450, 142220 https://doi.org/10.1016/j.electacta.2023.142220
Issue Date	2023-05-10
Doc URL	https://hdl.handle.net/2115/94215
Rights	© <2023>. This manuscript version is made available under the CC-BY-NC-ND 4.0 license http://creativecommons.org/licenses/by-nc-nd/4.0/
Rights(URL)	https://creativecommons.org/licenses/by-nc-nd/4.0/
Type	journal article
File Information	Electrochim. Acta 450 142220 .pdf

Hokkaido University Collection of Scholarly and Academic Papers : HUSCAP

Title: Elucidation of electrochemical and morphological difference of carbon steel corroded in aqueous chloride solutions at low temperatures.

Tong Shen [a, *], Masatoshi Sakairi [b]

[a] Family name: Shen, Given name: Tong

Affiliation address: Graduate School of Engineering, Hokkaido University, Kita-13, Nishi-8, Kita-ku, Sapporo, Hokkaido 060-8628, Japan

E-mail: t.shen.b8@outlook.com

[b] Family name: Sakairi, Given name: Masatoshi

Affiliation address: Faculty of Engineering, Hokkaido University, Kita-13, Nishi-8, Kita-ku, Sapporo, Hokkaido 060-8628, Japan

E-mail: msakairi@eng.hokudai.ac.jp

* corresponding author

Abstract

In humid continental climate areas, brine rejection results in the metal being exposed to higher and changing concentrations of chloride ions derived from precipitation. In this study, the corrosion behavior of carbon steel in different conditions especially in high chloride ions concentrations and at low temperature were investigated via electrochemical methods Liner Sweep voltammetry (LSV), Electrochemical Impedance Spectroscopy (EIS), and surface analysis. The results indicate that the dominant factor in affecting current in the temperature range from 20 ºC to 0 ºC is different from that in the range from 0 ºC to -20 ºC. It was found that the charge transfer reactions were inhibited in high concentrated NaCl solutions, and corrosion morphology changed from pitting corrosion to general corrosion due to the frequent occurrence of passive film destruction induced by chloride ions. Furthermore, in addition to the common corrosion products found at both 0 ºC and 20 ºC, Fe_3O_4 / γ-Fe_2O_3 was detected only at 20 ºC.

Key word: Low temperature, Carbon Steel, Corrosion, EIS, LSV

1. Introduction

The widespread use of carbon steel in infrastructure construction makes atmospheric corrosion of carbon steel a long-standing concern [1][2][3][4]. The corrosion induced by chloride ions is ineluctable when studying atmospheric corrosion. Precipitation in coastal areas is usually enriched with a higher concentration of chloride ions compared to inland areas, and deposition of salt particles on metal will lead to a harsh corrosive environment for metallic infrastructure in coastal areas [5][6][7][8].

Humid continental climate areas such as Hokkaido in Japan often have high precipitation and long periods of sub-zero temperature in winter, which is a different corrosive environment compared to subtropical and tropical climate areas that many previous studies focused on [9][10][11][12]. When the temperature drops below the freezing point of the aqueous solution, brine rejection occurs simultaneously during the freezing process. The water in the aqueous solution begins to preferentially freeze, and the salts in the solution are excluded from the ice crystals. This increases the chloride ion concentration in the remaining liquid phase, eventually reaching a saturated state [13][14][15]. This also results in the metal being exposed to higher and ever-changing concentration of chloride ion with temperature. Therefore, the change in chloride ion concentration also needs to be considered when investigating the corrosion behavior of carbon steel in low temperature environments, especially in nearly saturated salt solution [16].

Atmospheric corrosion of metallic materials is a coupled electrochemical reaction. Oxygen

Reduction Reaction (ORR) in neutral aqueous solution is of great concern as the rate of electrons consumed in this cathodic reaction determines the generation of electrons in the anodic reaction. Properties of the electrolyte such as dissolved oxygen concentration [17][18][19], diffusion coefficient [20][21][22] and viscosity [23] are often affected by decrease in temperature. Variations in these parameters greatly affect the oxygen diffusion-limited current, which is typically obtained from the ORR reaction [24].

In this study, the corrosion behavior of carbon steel in chloride ion aqueous solution with concentrations from 1 mass% to 20 mass% was investigated. Corrosion temperatures were set at -20 ºC to 20 ºC. Corrosion behavior under all conditions were investigated by performing electrochemical measurements (LSV and EIS), surface observations and analysis (SEM, XRD, AFM and EDS).

2. Experimental

2.1 Conditions

Carbon steel plates of Steel Plate Cold Commercial (SPCC) (Compositions in mass%: C = 0.045; Mn = 0.18; P = 0.01; S<0.01; and Fe-balance) were used in the present study. Aqueous electrolyte with 1, 5,10, and 20 mass% NaCl were prepared at 0 ºC and 20 ºC under atmospheric pressure. Two additional tests were operated in 20 mass% NaCl at -10 ºC and -20 ºC (supercooling state), based on the phase diagram of the NaCl – water binary system shown in Fig. 1 [25][26]. Temperature was maintained by a Constant-Low-Temperature water circulator (LBX-500, AXEL) with an error of $\pm$0.05 ºC.

2.2 Electrochemical measurement

Electrochemical measurements were performed under all conditions using a potentiostat (HZ-7000, HOKUTO DENKO). A three-electrode cell was employed with a Pt plate as the counter electrode (CE) and a saturated KCl-Ag/AgCl electrode (SSE) as the reference electrode (RE). Working electrodes (WE) were prepared by the following procedure. One side of the carbon steel plate was soldered to a lead wire and mounted in epoxy resin with an exposure area of 4 cm^2. A schematic diagram of the three-electrode cell is shown in Fig. 2. Before the electrochemical measurement, the surface was mechanically ground up to #4000 successively by SiC abrasive papers, followed by ultrasonically rinsing with ethanol (99.5%) and highly purified water (18.2 MΩ cm) for 300 s in that sequence.

The positive and negative direction polarization curves were initiated separately after 1 h Open Circuit Potential (OCP) was monitored. The potential scan rates of both anodic and cathodic polarization curves were set at 20 mV min^{-1}. The applied potential scan range was set to begin from OCP and to end at the potential with current density of 10^{-3} $A \cdot cm^{-2}$. For an Electrochemical Impedance Spectroscopy (EIS) measurements, sinewave perturbation amplitude of 10 mV peak-to-peak at OCP was carried out, and 10 points per decade were measured in the frequency range of 10 kHz to 10 mHz. The experimental data were analyzed by specialized analysis software (EIS, HOKUTO DENKO). The EIS measurements were carried out with samples after different durations of immersion.

2.3 Immersion tests and surface analysis

Specimens were cut into 10×10× 0.7 mm for immersion tests and surface analysis. The surface was

mechanically ground up to #4000 successively by SiC abrasive papers and polished with 0.25 μm polycrystalline diamonds, then ultrasonically rinsed in ethanol and distilled water for 300 s. Immersion tests were carried out in all electrochemical measurements condition for 48 h and performed with triplicate tests. All the immersion tests were open to the atmosphere. The mass of the specimen was measured with a microbalance (MX5 microbalance, METTLER TOLEDO) prior to immersion and after removing the corrosion product by ultrasonic cleaning following 48 h immersion.

The morphology of the 48 h corroded specimens was observed using Scanning Electron Microscope (SEM, JEOL, JSM-6510LA) with an accelerating voltage of 10 kV, and an SEM equipped with Energy-dispersive X-ray spectroscope (EDS) with an accelerating voltage of 15 kV was used to analyze the elemental compositions of different surface regions. The corroded specimens surface morphology was also investigated via Atomic Force Microscope (AFM, HITACHI, SPA-400), and the crystal structures and chemical compositions of corrosion products were analyzed by X-ray diffraction (XRD, Rigaku, Smart Lab).

2.4 Immersion tests

Yellowish rusts were observed in the samples after 48 h of immersion, and the corrosion products were not considered to adhere to the surface of the metal firmly since they can be removed after ultrasonic cleaning. The mass loss (WL) was calculated as a percentage of mass loss via Eq. (1)

$$\mathrm{WL} = \frac{W_0 - W_1}{W_0} \times 100 \qquad (1)$$

wherein W_0(g) is the mass of the specimen before immersion, and W_1(g) is the mass of the specimen

after removing the corrosion product following 48 h immersion tests. As the mass loss in 20 mass% NaCl at -20 ºC was minute, significant error is present so the mass loss in this condition is not exhibited.

3. Results and discussions

3. 1 Open Circuit Potential and Polarization curves

Fig. 3 shows the changes in OCP as a function of time during the initial 3600 s, and all the potentials reached a steady value after immersion. Although the OCPs in all concentrations show a similar value at 20 ºC, the OCP ennobles with decrease in concentration at 0 ºC. In addition, OCP after 1 h immersion increases with decreasing temperature, which was observed at all concentrations.

Potentiodynamic polarization curves measured in all concentrations at 0 ºC and 20 ºC, and in temperature range from 20 ºC to -20 ºC are separately shown in Figs. 4 (a) and (b). The sharp increases in current densities as overpotential increase in the anodic polarization curves from 1 mass% to 20 mass% represent the dissolution of iron and is described as:

$$Fe \rightarrow Fe^{2+} + 2e^{-} \quad (2)$$

In the cathodic polarization curves, part, two reactions can be identified: A plateau region at the initiation part, which is considered as the oxygen reduction reaction (ORR) and mainly governed by the mass transfer of oxygen (Reaction.3), a hydrogen evolution reaction follows stepwise at more negative potentials (Reaction.4).

$$O_2 + 2H_2O + 4e^{-} \rightarrow 4OH^{-} \quad (3)$$

$$2H_2O + 2e^{-} \rightarrow H_2 + 2OH^{-} \quad (4)$$

The oxygen diffusion-limited current densities derived from the extrapolation of flat region in the cathodic polarization curves were plotted as a function of concentrations at 0 ºC and 20 ºC (Fig. 5(a)).

As the working electrode was set vertically, the local limiting current density at any height X is calculated by Levich [27]:

$$i_X = 0.382nFv^{-\frac{1}{4}}D^{\frac{3}{4}}g\alpha^{\frac{1}{4}}X^{-\frac{1}{4}}c_b^{\frac{5}{4}} \quad (5)$$

Where n is the number of moles of electrons transferred in the half reaction, F is the Faraday constant(C mol^{-1}), v is the dynamic viscosity, D is the diffusion coefficient, g is the acceleration of gravity, α is the density coefficient which defined as:

$$\alpha = \frac{1}{\rho_b}\left(\frac{\partial\rho}{\partial c}\right) \approx \frac{\rho_b - \rho_s}{\rho_b(c_b - c_s)} \quad (6)$$

In this study, C_b and C_s are the concentration of oxygen in bulk solution and at the electrode surface (assumed to be zero), ρ_b and ρ_s are the fluid density in bulk solution and at the electrode surface. Assuming the electrode height is X_0, the average local limiting current density on the electrode surface can be derived as in equation (7).

$$i_{avg} = \frac{1}{X_0}\int_0^{X_0} i_X \cdot dX = \frac{4}{3}i_{X_0} = 0.382nFv^{-\frac{1}{4}}D^{\frac{3}{4}}gX_0^{-\frac{1}{4}}c_b\left(\frac{\rho_b - \rho_s}{\rho_b}\right)^{\frac{1}{4}} \quad (7)$$

It was reported that the concentration of dissolved oxygen, diffusion coefficient, and reciprocal of viscosity v^{-1} exhibit a negative dependence with the increase in NaCl concentration [19][20][21][22][23]. Additionally, as the difference of fluid density ($\rho_b - \rho_s$) is attributed to the dissolved oxygen depletion, ($\rho_b - \rho_s$) is directly related to the dissolved oxygen concentration. So, $\frac{\rho_b - \rho_s}{\rho_b}$ will decrease when the NaCl concentration increases or temperature increases.

From the relationship between each variable and the solution concentration, it can be seen that an increase in the solution concentration leads to a decrease in the limiting current density at a constant temperature, which is consistent with Fig. 5 (a). The magnitude of oxygen diffusion-limited current changes with concentration at 0 ºC is significantly greater than at 20 ºC. As temperature decreases, v^{-1} and D exhibit a decreasing trend, while c_b and density coefficient exhibits an opposite trend. This indicates that effects of c_b and density coefficient are dominant in the temperature change from 20 ºC to 0 ºC. Fig. 5 (b) shows the change of oxygen diffusion-limited current density as a function of temperature in 20 mass%. Hence, it can be seen that in the temperature decrease from 20 ºC to 0 ºC, the limiting current density is governed by dissolved oxygen concentration. A decreasing trend exhibits when the temperature decrease occurs below 0 ºC, which indicates the viscosity and diffusion coefficient play a more important role in the limiting current density.

The corrosion current densities calculated by mass loss (j_{mass}) are shown in Table 1 with a comparison of oxygen diffusion-limited current densities ($j_{\text{lim, O}_2}$). At 20 ºC, j_{mass} is similar to $j_{\text{lim, O}_2}$, however, the latter is much higher than the former at 0 ºC in all concentrations and below 0 ºC in 20 mass% cases, especially in high concentrations. From the current densities calculated from real mass loss, ORR might not be the rate-determining step at and below 0 ºC, and corrosion prediction from a short time polarization measurement cannot work well in these conditions.

3. 2 EIS measurements

EIS results of different conditions with time are performed as Bode plots in Fig. 6. One peak in

Bode-phase angle plots indicates that one time-constant equivalent circuit would be considered to fit the EIS data as shown in Figs. 6 (b), (d), (f), and (h). A Randles' equivalent circuit with a charge transfer resistance (R_{ct}) in parallel with a constant phase element (CPE) and an electrolyte resistance (R_s) connected in series (Fig. 6 (i)) corresponds to the obtained EIS data. The fitted results with Chi-square

(χ^2) parameter are listed in Table 2. The impedance response of the electrochemical system was proposed by Zoltowski [28] as,

$$Z = R_e + \frac{R_{ct}}{1 + Q(j2\pi f)^n R_{ct}} \quad (8)$$

Where j is the imaginary number such that $j^2 = -1$, Q ($s^n \Omega^{-1}$ cm^{-2}), f is the frequency and n are the distribution elements of CPE. When n = 1, CPE is a pure capacitor and when n = 0, CPE is a pure resistor. The effective capacitance is expressed collectively by all elements of this circuit as [29][30]:

$$C_{eff} = Q^{\frac{1}{n}} \left(R_e^{-1} + R_{ct}^{-1} \right)^{\frac{n-1}{n}} \quad (9)$$

The conductance G (= $1/R_{ct}$) represents the magnitude of corrosion rate since the conductance is proportional to the corrosion current. The values of charge transfer conductance G after 1 h and 48 h immersion are plotted in Fig. 7.

It is found that G exhibited a negative dependence with an increase in concentration after 1 h immersion at 20 ºC, which is more noticeable after 48 h of immersion (Fig. 7 (a)). At 0 ºC, G does not change significantly in 1, 5 and 10 mass% conditions after 1 h, while after 48 h, 5 and 10 mass% deteriorated conspicuously and showed a similar value of nearly 50% of that in 1 mass%.

In addition, G calculated in 20 mass% at 20 ºC and 0 ºC have the lowest value in all concentrations, which indicates that the charge transfer process is inhibited in a denser solution. A diagram of G as a function of temperature in 20 mass% shown in Fig. 7 (b) also exhibits a temperature dependency at immersion time for 48 h, though the value of G at 1 h is close at these concentrations. It can be seen that the variation of G after 48 h of immersion corresponds to the calculated value of mass loss percentage plotted with different conditions shown in Fig. 8

The decrease of G with time at and below 0 ºC in 5, 10 and 20 mass% cases suggests that the corrosion rate is hindered in the immersion process, and the main reason for the decline of corrosion rate over time is usually attributed to the decrease in transfer of reactants and products hindered by corrosion products. This is consistent with the difference between the oxygen diffusion-limited current after 1 h immersion and corrosion current density calculated from mass loss. Additionally, the decrease of *n* value is shown in all conditions. As CPE converted into a Warburg diffusive element when n = 0.5, a lower *n* value ($0.5 < n < 1$) suggests the corrosion tends to be affected by the diffusion process, which is thought to be caused by corrosion products formed in the immersion.

3. 3 Morphology of rust layers

The microstructural characteristics of all samples with the rust layer were investigated by SEM. Figs. 9 (a) - (h) show the rust layers formed on carbon steel after 48 h of immersion. Morphologies of the rust layer including floral structure and solid spheroids were observed on the surface of samples. The morphologies related to various ferric oxide-hydroxide and ferrous ferric oxide which formed in the

continuous corrosion process were identified as crystalline phases γ-FeOOH (Lepidocrocite) and Fe_3O_4 (Magnetite) / γ-Fe_2O_3 reported in previous literatures [31][32][33]. Flowery structures (which are morphologically similar to γ-FeOOH) are considered to be the main corrosion product at all temperatures.

Compared to the rust layers formed on the samples immersed at 0 ºC, some small solid globular particles aggregated and adhered to the specimen surface could be seen at 20 ºC, which seems to correspond to the formation of Fe_3O_4 / γ-Fe_2O_3. XRD analyses were performed to verify the corrosion products.

As only minute amounts of corrosion products are generated at sub-zero temperatures, XRD analysis of samples immersed at -20 ºC do not offer meaningful insight. Therefore, only the samples immersed at 0 ºC and 20 ºC were analyzed. The XRD patterns shown in Fig. 10 indicates that γ-FeOOH exist under all conditions. Furthermore, Fe_3O_4 / γ-Fe_2O_3 are only detected on the specimens immersed at 20 ºC, which is consistent with the morphological discrepancy observed by SEM. Although it is difficult to differentiate between Fe_3O_4 and γ-Fe_2O_3 via XRD since their crystal structure is almost indistinguishable [31][34], the peaks of both γ-Fe_2O_3 and Fe_3O_4 can be attributed to Fe_3O_4 [35].

In many studies, products formed in the corrosion process were investigated. The corrosion process of carbon steel was considered as follows: at the initiation stage of corrosion, dissolved Fe^{2+} combined with OH^- ions (these ions derived from the electrochemical reactions (2)(3) on carbon steel) and form a gelatinous $Fe(OH)_2$ layer on the carbon steel. It must be recalled that $Fe(OH)_2$, if it really forms,

which may not be the case, is rapidly oxidized to a green rust (GR) compound. The GR compound may be in most cases the first solid phase to form [36][37]. For the sake of simplification, the term "$Fe(OH)_2$" is used in the following discussion and reactions instead of GR. The formation of $Fe(OH)_2$ via reaction (10):

$$Fe^{2+} + 2OH^- \leftrightharpoons Fe(OH)_2 \quad (10)$$

As the generated gelatinous $Fe(OH)_2$ shows solubility in water and the hydrolysis of Fe^{2+} is weak [38], the $Fe(OH)_2$ is unstable in an aqueous environment. When the concentration of Fe^{2+} is lower than an equilibrium state, the reaction (10) tends to occur in the left direction, and $Fe(OH)_2$ begins to form. Therefore, it can be considered that the oxidation of Fe^{2+} and $Fe(OH)_2$ always took place simultaneously in this study by [38][39]:

$$4Fe^{2+} + 8OH^- + O_2 + 2H_2O \rightarrow 4Fe(OH)_3 \quad (11)$$

or

$$6Fe^{2+} + 12OH^- + O_2 \rightarrow 2Fe_3O_4 + 6H_2O \quad (12)$$

Reaction (11) is induced by sufficient oxygen. In contrast, when there is slow aerial oxidation / insufficient oxygen supply, reaction (12) tends to happen. Further conversion to other crystalline phases after reaction (11) is shown in reaction (13):

$$Fe(OH)_3 \rightarrow FeOOH + H_2O \quad (13)$$

The disappearance of magnetite at low temperature is shown in Figs. 8 (b) (d) (f) (h), and this situation was also reported in other literature [40]. Since the transformation from gelatinous $Fe(OH)_2$

to magnetite occurs favorably in a situation where the supply of oxygen is limited, the dissolved oxygen concentration may be a dominant factor in explaining the morphological difference [41]. It can be considered that at 20 ºC, Fe^{2+} from anodic reaction tends to be subjected to partial oxidation as shown in reaction (12). On the other hand, Fe^{2+} was fully oxidated to Fe^{3+} at 0 ºC as according to reaction (11).

Additionally, the distribution of corrosion products at 20 ºC indicates that Fe_3O_4 forms favorably in the interface of steel substrate and FeOOH, which is commonly found in many corrosion studies in a chloride ion-containing environment [36][38]. H. Tamura [38] pointed out this phenomenon can be attributed to that the generation of Fe_3O_4 in the initial stage of corrosion. As Fe_3O_4 is electronically conductive, electric current will pass through the corrosion products containing Fe_3O_4, and the reduction of oxygen takes place on the outer side of these corrosion products. As a result, a de-aerated area between Fe_3O_4 and metal forms, hindering further oxidation of Fe_3O_4 [37][42].

3. 4 Surface morphology of different corrosion behavior

The SEM results of the samples after removing the corrosion products are exhibited in Figs. 11 and 12. It is apparent that corrosion occurred preferentially on some grains in all conditions. In addition, a considerable number of pits can be observed in 1 mass% cases (Figs. 11 (a) and (b)) but which could not be found in higher concentrations. While similar surface morphologies are observed in 1 mass%, the difference of the surface between 0 ºC and 20 ºC is evident in other concentrations.

The morphological discrepancy between different concentrations is also detected via AFM

observation. The 3D images of samples surface immersed in solutions at and below 0 ºC are shown in Fig. 13. The AFM also proved the occurrence of preferential corrosion. Moreover, the height difference at and below 0 ºC in 20 mass% are almost the same. The corrosion behavior at and below 0 ºC in 20 mass% seems similar, suggesting the corrosion rate in this concentration might not be affected by temperature decrease.

Fig. 14 shows the EDS point analysis of the sample immersed at -20 ºC in 20 mass%. The average atomic ratio of carbon were found to be 12.1% at grain boundary, 4.5% and 5.0% in surrounding areas. The high carbon content area in the grain boundaries is considered as cementite, and acts as cathode with respect to the adjacent low carbon content area (ferrite) [43][44][45]. The distribution of cementite induces the formation of localized-galvanic cells between areas of high and low carbon content in an aqueous solution. The galvanic action might result in selected dissolution of some grains.

There are many hypotheses of the pitting corrosion induced by chloride ions. H.H. Uhlig [46] proposed the chloride ions absorbed on metal will compete with the oxygen for absorption sites on the metal. A soluble species formed by chloride ions and metal will induce pitting corrosion. The penetration of chloride ions into the oxide film and their reaction with Fe^{3+} inducing the breakdown of the oxide film has also been experimentally proven by Engell and Stolica [47]. According to Point Defect Model (PDM) [48][49][50], the chloride ions play an influential catalytic role in the process of destroying the protective oxide film via occupation behavior with oxygen vacancy, and then inducing the localized corrosion. In summary, chloride ions penetrate and destroy the structure of the oxide film,

leading to some local defects in the oxide film and ultimately pitting corrosion. Unfortunately, almost all the theories of damage to oxide films induced by chloride ions have not been proven directly.

It can be considered that when the chloride ions concentration is relatively low, the chloride ion-induced passive film destruction tends to occur partially, leading to significant pitting corrosion. By contrast, frequent occurrence of local destruction of passive film will cause uniform corrosion instead of pitting corrosion in higher chloride ion concentration, and localized micro-galvanic corrosion occurs simultaneously.

4. Conclusions

By electrochemical measurements and surface analysis, the corrosion behavior of SPCC at low temperatures with different concentrations of NaCl was investigated and compared to 20 ºC cases. Mass losses were calculated to corroborate electrochemical results. The difference of corrosion products and the surface morphology after removing the corrosion products were studied. The main conclusions drawn from this study are as follows:

1. According to the oxygen diffusion-limited current densities derived from the cathodic polarization curves, the concentration of oxygen in bulk solution is the dominant factor in the temperature change from 20 ºC to 0 ºC. Additionally, the viscosity and diffusion coefficient play more important roles in limiting current density when the temperature decrease below 0 ºC.
2. The main difference between corrosion products at 0 ºC and 20 ºC is that Fe_3O_4 / γ-Fe_2O_3 appeared only at the latter. The appearance of Fe_3O_4 / γ-Fe_2O_3 might be attributed to the

limitation of oxygen supply.

3. After 48 h of immersion, the charge transfer conductance decreased with increasing concentration of NaCl at 0 ºC and 20 ºC, which means the charge transfer reaction is inhibited in a high concentrated solution. In addition, a temperature dependency of immersion time for 48 h was exhibited in 20 mass% solutions. However, it could not be seen at the initiation stage of immersion.
4. In 1 mass% NaCl, the passive film is only partially destroyed by the low concentration of chloride ions, hence significant pitting corrosion is observed. However, pitting corrosion was not observed in higher NaCl concentrations. Localized corrosion plays a significant role in corrosion process after the passive film is destroyed.

Declaration of Competing Interest

The authors declare there are no competing declarations of interests.

Acknowledgements

Surface observation and analysis in this work were conducted at Laboratory of XPS analysis, Joint-use facilities, Hokkaido University, supported by “Advanced Research Infrastructure for Materials and Nanotechnology in Japan (ARIM)” of the Ministry of Education, Culture, Sports, Science and Technology (MEXT). Proposal Number JPMXP1222HK0032.

Reference

[1] K. Otani, M. Sakairi, Effects of metal cations on corrosion of mild steel in model fresh water, Corros. Sci. 111 (2016) 302–312.

[2] R. Rizzo, S. Gupta, M. Rogowska, R. Ambat, Corrosion of carbon steel under CO_2 conditions: effect of $CaCO_3$ precipitation on the stability of the $FeCO_3$ protective layer, Corros. Sci. 162 (2020) 108214.

[3] B. Hou, X. Li, X. Ma, C. Du, D. Zhang, M. Zheng, W. Xu, D. Lu, F. Ma, The cost of corrosion in China, npj. Mater. Degrad. 1 (2017) 4.

[4] L. Li, M. Sakairi, Effects of Metal Cations on Corrosion Morphology of Carbon Steel in Model Fresh Water, Zairyo-to-Kankyo. 71 (2022) 208-212.

[5] C.E. Junge, R.T. Werby, The concentration of chloride, sodium, potassium, calcium, and sulfate in rain water over the united states, J. Atmos. Sci. 15 (1958) 417–425.

[6] A.Y. Shcherbina, L.D. Talley, D.L. Rudnick, Direct Observations of North Pacific Ventilation: Brine Rejection in the Okhotsk Sea, Science. 302 (2003) 1952-1955

[7] A.V. Holden, Concentration of Chloride in Fresh Waters and Rain Water, Nature. 192 (1961) 961–962.

[8] D. Beysens, C. Ohayon, M. Muselli, O. Clus, Chemical and biological characteristics of dew and rain water in an urban coastal area (Bordeaux, France), Atmospheric Environ. 40 (2006) 3710-3723.

[9] Y. Ma, Y. Li, F. Wang, The atmospheric corrosion kinetics of low carbon steel in a tropical marine environment, Corros. Sci. 52 (2010) 1796-1800.

[10] S.J. Oh, D.C. Cook, H.E. Townsend, Atmospheric corrosion of different steels in marine, rural and industrial environments, Corros. Sci. 41 (1999) 1687-1702.

[11] D.D.N. Singh, S.Yadav, J.K. Saha, Role of climatic conditions on corrosion characteristics of structural steels, Corros. Sci. 50 (2008) 93-110.

[12] J.J.S. Rodríguez, F.J. Hernández, J.E.G. González, The effect of environmental and meteorological variables on atmospheric corrosion of carbon steel, copper, zinc and aluminium in a limited geographic zone with different types of environment, Corros. Sci. 45 (2003) 799-815.

[13] P. Rohatgi, C. Adams, Ice–Brine Dendritic Aggregate formed on Freezing of Aqueous Solutions, J. Glaciol. 6 (1967) 663-679.

[14] I. Tsironi, D. Schlesinger, A. Späh, L. Eriksson, M. Segad, F. Perakis, Brine rejection and hydrate formation upon freezing of NaCl aqueous solutions, Phys. Chem. Chem. Phys. 22 (2020) 7625-7632.

[15] L. Vrbka, P. Jungwirth, Brine Rejection from Freezing Salt Solutions: A Molecular Dynamics Study, Phys. Rev. Lett. 95 (2005) 148501.

[16] A. Kazuhisa, N. Tatsuki, Visualization of Coupling Current and Immersion Potential of Iron Surface Corroding Beneath the Ice in the Temperature Cycling under the Freezing Point, ISIJ Int. 62 (2022) 1930-1936.

[17] R.F. Weiss, The solubility of nitrogen, oxygen and argon in water and seawater, Deep-Sea Res. Oceanogr. Abstr. 17 (1970) 721–735.

[18] C.G. MacArthur, Solubility of Oxygen in Salt Solutions and the Hydrates of These Salts, J. Phys. Chem. 20 (1915) 495–502.

[19] B. Debelius, A. Gómez-Parra, J.M. Forja, Oxygen solubility in evaporated seawater as a function of temperature and salinity, Hydrobiologia. 632 (2009) 157–165.

[20] A.J. Van Stroe, L.J.J. Janssen, Determination of the diffusion coefficient of oxygen in sodium chloride solutions with a transient pulse technique, Anal. Chim. Acta. 279 (1993) 213–219.

[21] M. Jamnongwong, K. Loubiere, N. Dietrich, G. Hébrard, Experimental study of oxygen diffusion coefficients in clean water containing salt, glucose or surfactant: Consequences on the liquid-side mass transfer coefficients, Chem. Eng. J. 165 (2010) 758–768.

[22] S. Tanaka, S. Kastens, S. Fujioka, M. Schlüter, K. Terasaka, Mass transfer from freely rising microbubbles in aqueous solutions of surfactant or salt, Chem. Eng. J. 387 (2020) 121246

[23] J. Kestin, H.E. Khalifa, R.J. Correia, Tables of the dynamic and kinematic viscosity of aqueous NaCl solutions in the temperature range 20–150 °C and the pressure range 0.1–35 MPa, J. Phys. Chem. Ref. Data. 10 (1981) 71–88.

[24] V.G. Levich, No Title, Acta physicochim, Urss. 17 (1942) 257.

[25] Y. Farnam, D. Bentz, A. Sakulich, D. Flynn, J. Weiss, Measuring Freeze and Thaw Damage in Mortars Containing Deicing Salt Using a Low Temperature Longitudinal Guarded Comparative Calorimeter and Acoustic Emission (AE-LGCC), Adv. Civ. Eng. Mater. 3 (2014) 316-337.

[26] W. M. Haynes, CRC Handbook of Chemistry and Physics, 95th ed., CRC Press, Boca Raton, 2014.

[27] C.W. Tobias, M. Eisenberg, C.R. Wilke, Fiftieth Anniversary: Diffusion and Convection in Electrolysis—A Theoretical Review, J. Electrochem. Soc. 99 (1952) 359C.

[28] P. Zoltowski, On the electrical capacitance of interfaces exhibiting constant phase element behaviour, J. Electroanal. Chem. 443 (1998) 149–154.

[29] G.J. Brug, A.L.G. van den Eeden, M. Sluyters-Rehbach, J.H. Sluyters, The analysis of electrode impedances complicated by the presence of a constant phase element, J. Electron. Chem. Interfa. Electrochem. 176 (1984) 275-295.

[30] B. Hirschorn, M.E. Orazem, B. Tribollet, V. Vivier, I. Frateur, M. Musiani, Determination of effective capacitance and film thickness from constant-phase-element parameters, Electrochim. Acta. 55 (2010) 6218–6227.

[31] D. de la Fuente, I. Díaz, J. Simancas, B. Chico, M. Morcillo, Long-term atmospheric corrosion of mild steel, Corros. Sci. 53 (2011) 604-617.

[32] Ph. Dillmann, F. Mazaudier, S. Hoerlé, Advances in understanding atmospheric corrosion of iron: I. Rust characterisation of ancient ferrous artefacts exposed to indoor atmospheric corrosion, Corros. Sci. 46 (2004) 1401–1429.

[33] J. Yang, Y. Lu, Z. Guo, J. Gu, C. Gu, Corrosion behaviour of a quenched and partitioned medium carbon steel in 3.5wt.% NaCl solution, Corros. Sci. 130 (2018) 64-75.

[34] D.C. Cook, Spectroscopic identification of protective and non-protective corrosion coatings on steel structures in marine environments, Corros. Sci. 47 (2005) 2550-2570.

[35] Y.S. Kang, S. Risbud, J.F. Rabolt, P. Stroeve, Synthesis and Characterization of Nanometer-Size Fe_3O_4 and γ-Fe_2O_3 Particles, Chem. Mater. 8 (1996) 2209–2211.

[36] Ph. Refait, A.M. Grolleau, M. Jeannin, C. Rémazeilles, R. Sabot, Corrosion of carbon steel in marine environments: role of the corrosion product layer, Corros. Mater. Degrad. 1 (2020) 198-218.

[37] Ph. Refait, A.-M. Grolleau, M. Jeannin, E. François, R. Sabot, Localized corrosion of carbon steel in marine media: galvanic coupling and heterogeneity of the corrosion product layer, Corros. Sci. 111 (2016) 583-595.

[38] H. Tamura, The role of rusts in corrosion and corrosion protection of iron and steel, Corros. Sci. 50 (2008) 1872–1883.

[39] T. Misawa, K. Asami, K. Hashimoto, S. Shimodaira, The mechanism of atmospheric rusting and the protective amorphous rust on low alloy steel, Corros. Sci. 14 (1974) 279-289.

[40] K.Inoue, S.K. Kwon, K. Kimijima, K. Kanie, A. Muramatsu, K. Shinoda, S. Suzuki, Y. Waseda, Analysis of Iron Oxyhydroxides and Oxides Converted from Green Rust in Aqueous Solution, ISIJ Int. 47 (2007) 453–457.

[41] T. Misawa, K. Hashimoto, S. Shimodaira, The mechanism of formation of iron oxide and oxyhydroxides in aqueous solutions at room temperature, Corros. Sci. 14 (1974) 131-149.

[42] Ph. Refait, M. Jeannin, R. Sabot, H. Antony, S. Pineau, Corrosion and cathodic protection of carbon steel in the tidal zone: Products, mechanisms and kinetics, Corros. Sci. 90 (2015) 375-382.

[43] Y. Sun, H. Fujii, Effect of abnormal grain growth on microstructure and mechanical properties of friction stir welded SPCC steel plates, Mater. Sci. Eng. A. 694 (2017) 81–92.

[44] K. Yamaguchi, H. Adachi, N. Takakura, Effects of Plastic Strain and Strain Path on Young's Modulus of Sheet Metals, Met. Mater. 4 (1998) 420-425.

[45] H.H. Uhlig, R.W. Revie, Corrosion and Corrosion Control, third ed., John Wiley and Sons, New York, 1991.

[46] H.H. Uhlig, Adsorbed and reaction-product films on metals, J.Electrochem. Soc. 97 (1950) 215C-220C.

[47] H.J. Engell, N.D. Stolica, Untersuchungen über Lochfraß an passive Elektroden aus unlegiertem Stahl in chlorionenhaltiger Schwefelsäure, Arch. Eisenhütten.Wes. 30 (1959) 239-248

[48] D.D. Macdonald, The Point Defect Model for the Passive State, J. Electrochem. Soc. 139 (1992) 3434.

[49] K. Heusler, G. Cartledge, The influence of iodide ions and carbon monoxide on the anodic dissolution of active iron, J. Electrochem. Soc. 108 (1961) 732–740.

[50] D.D. Macdonald, X. Lei, Theoretical Interpretation of Anion Size Effects in Passivity Breakdown, J. Electrochem. Soc. 163 (2016) 738–744.

Table.1

Oxygen diffusion limited current densities evaluated from polarization curves compared with corrosion current densities calculated from mass loss.

Concentration (mass%)	Temperature (ºC)	j_{lim,O_2}(μA·cm^{-2})	j_{mass}(μA·cm^{-2})
1	20	11(±0.7)	9.4(±0.2)
	0	11(±1.7)	7.8(±0.6)
5	20	8.4(±1.0)	8.4(±0.4)
	0	11(±1.1)	4.2(±0.2)
10	20	7.1(±0.4)	6.4(±0.0)
	0	9.8(±0.6)	3.8(±0.8)
20	20	4.1(±0.4)	3.1(±0.1)
	0	5.5(±0.5)	1.1(±0.1)
	-10	4.4(±0.5)	0.5(±0.2)
	-20	4.0(±0.1)	-

Table.2

EIS fitting results for various immersion time in all conditions

1 mass%	20 ºC			0 ºC		
	1 h	24 h	48 h	1 h	24 h	48 h
R_s (Ω)	8.7	9.3	9.3	15.1	14.7	14.5
R_{ct} (Ω·cm^2)	612	527	507	986	807	727
C_{eff} (μF·cm^{-2})	616	1710	1740	451	937	940
n	0.85	0.79	0.76	0.84	0.72	0.70
χ^2(10^{-2})	0.25	0.29	0.29	0.10	0.02	0.12
5 mass%	20 ºC			0 ºC		
	1 h	24 h	48 h	1 h	24 h	48 h
R_s (Ω)	1.4	1.7	1.8	4.0	3.4	3.4
R_{ct} (Ω·cm^2)	626	631	686	1120	1500	1500
C_{eff} (μF·cm^{-2})	483	594	657	450	602	597
n	0.84	0.84	0.82	0.87	0.80	0.78
χ^2(10^{-2})	0.10	0.19	0.12	0.23	0.10	0.29
10 mass%	20 ºC			0 ºC		
	1 h	24 h	48 h	1 h	24 h	48 h
R_s (Ω)	1.0	1.1	1.2	1.7	1.4	1.4
R_{ct} (Ω·cm^2)	935	1070	1020	1150	1400	1530
C_{eff} (μF·cm^{-2})	209	405	502	304	343	352
n	0.81	0.81	0.79	0.86	0.81	0.80
χ^2(10^{-2})	0.18	0.02	0.06	0.32	0.07	0.05
20 mass%	20 ºC			0 ºC		
	1 h	24 h	48 h	1 h	24 h	48 h
R_s (Ω)	0.7	0.7	0.7	1.2	1.3	1.3
R_{ct} (Ω·cm^2)	1920	1710	1700	1700	2410	2460
C_{eff} (μF·cm^{-2})	221	490	641	278	324	353
n	0.83	0.81	0.80	0.84	0.84	0.83
χ^2(10^{-2})	0.18	0.23	0.39	0.19	0.07	0.11
20 mass%	-10 ℃			-20 ℃		
	1 h	24 h	48 h	1 h	24 h	48 h
R_s (Ω)	1.5	1.5	1.5	2.2	2.3	2.2
R_{ct} (Ω·cm^2)	2460	2850	2970	3000	3690	3890
C_{eff} (μF·cm^{-2})	240	321	321	239	376	416

n	0.86	0.85	0.85	0.88	0.84	0.82
$\chi^2(10^{-2})$	0.11	0.11	0.07	0.59	0.12	0.13

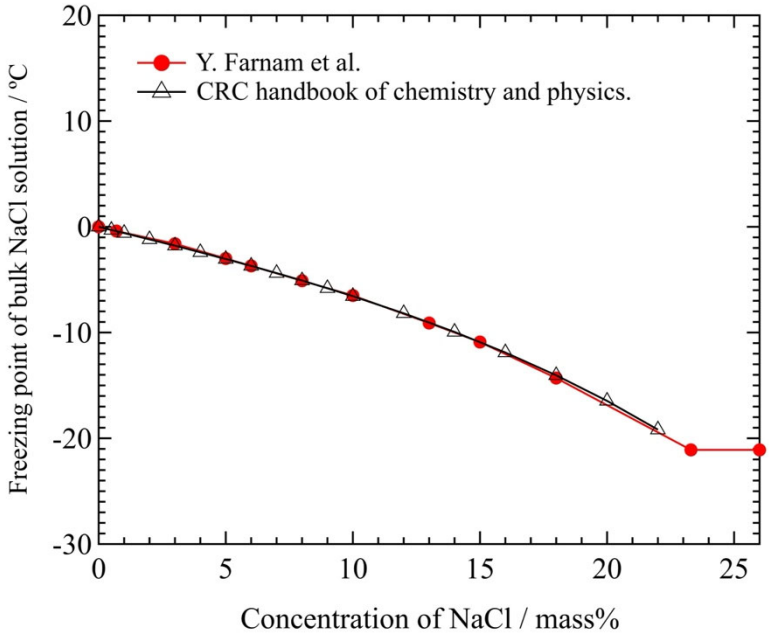


Fig. 1. Phase diagram of the NaCl – water binary system.

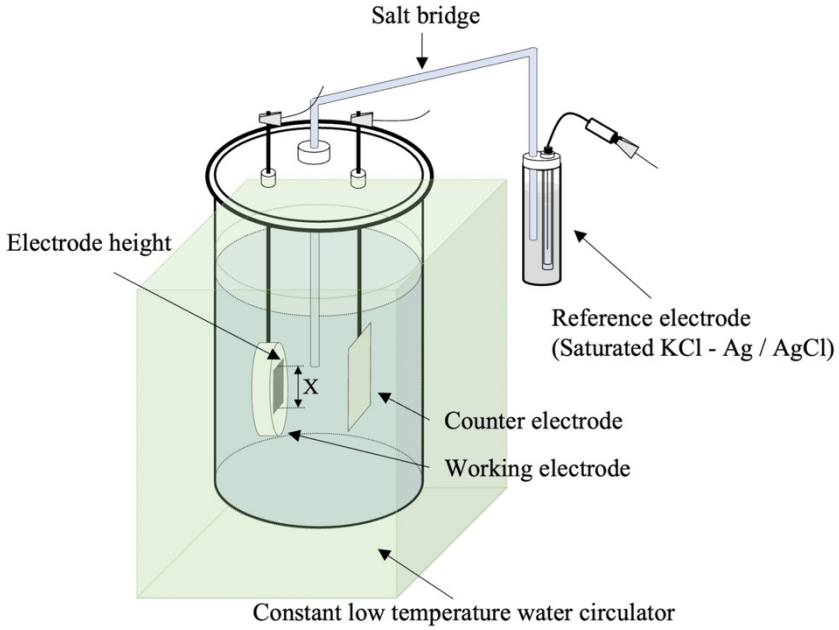


Fig. 2. Schematic drawing of experimental cell.

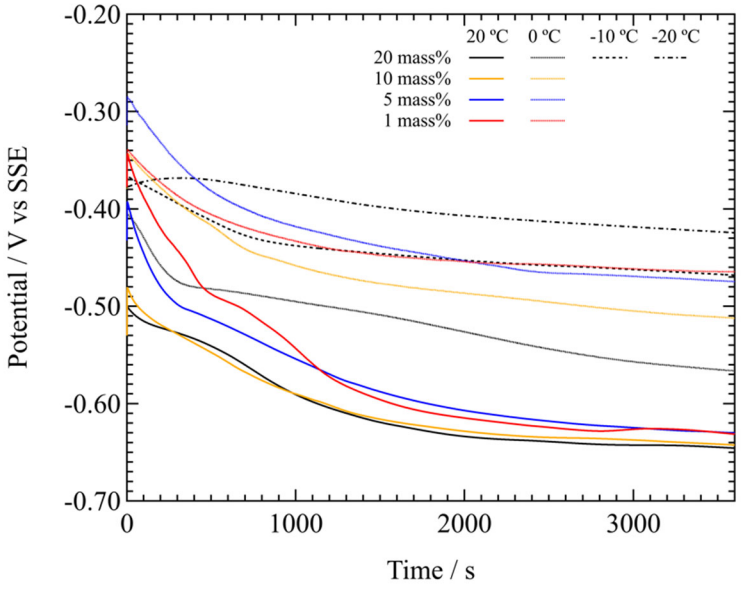


Fig. 3. Changes in OCP as a function of time for carbon steel in 1, 5, 10 and 20 mass% NaCl solutions with different temperatures.

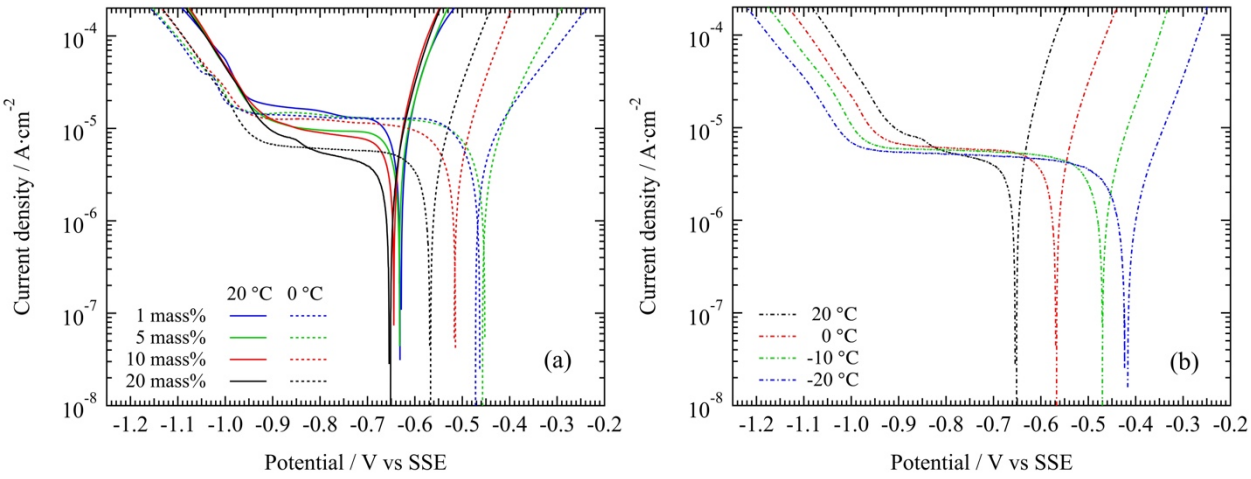


Fig. 4. Polarization curves of carbon steel in NaCl solutions with different concentrations and temperature: (a) at 20 ºC and 0 ºC in 1, 5, 10 and 20 mass%; (b) from 20 ºC ~ -20 ºC in 20 mass%.

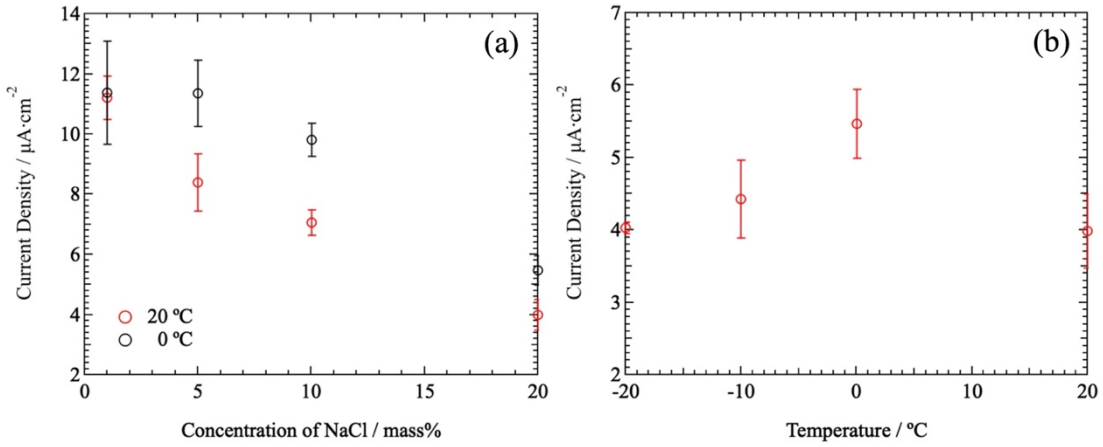


Fig. 5. Changes in oxygen diffusion-limited current density with different concentrations or temperatures; (a) at 20 ºC and 0 ºC in 1, 5, 10 and 20 mass%; (b) from 20 ºC ~ -20 ºC in 20 mass%.

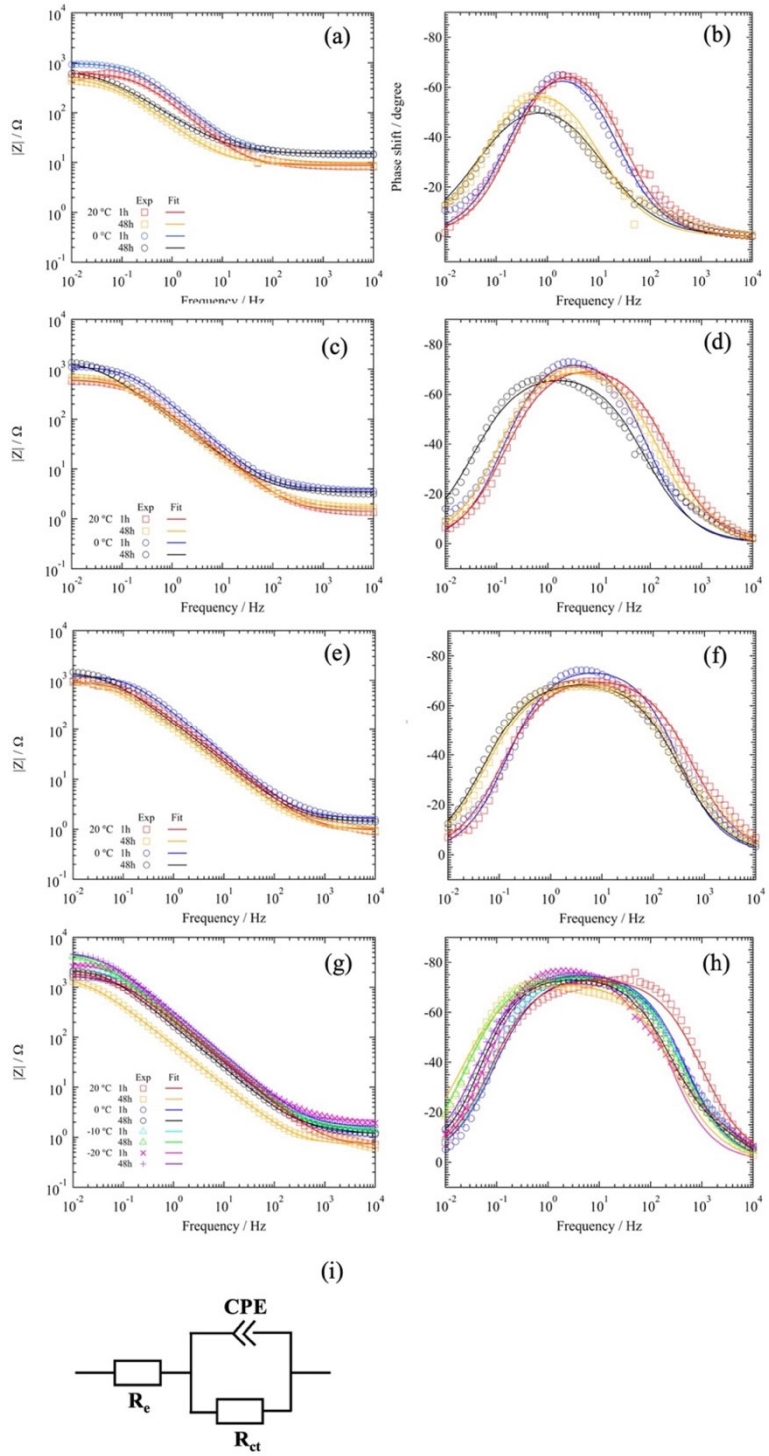


Fig. 6. Bode diagram of impedance ((a) 1 mass%, (c) 5 mass%, (e) 10 mass%, (g) 20 mass%) and phase shift plots ((b) 1 mass%, (d) 5 mass%, (f) 10 mass%, (h) 20 mass%) containing experimental (points) and fitting (solid lines) results obtained for the carbon steel immersed in the NaCl solution for 1 h and 48 h immersion. All the experimental data fitted by equivalent circuit (i).

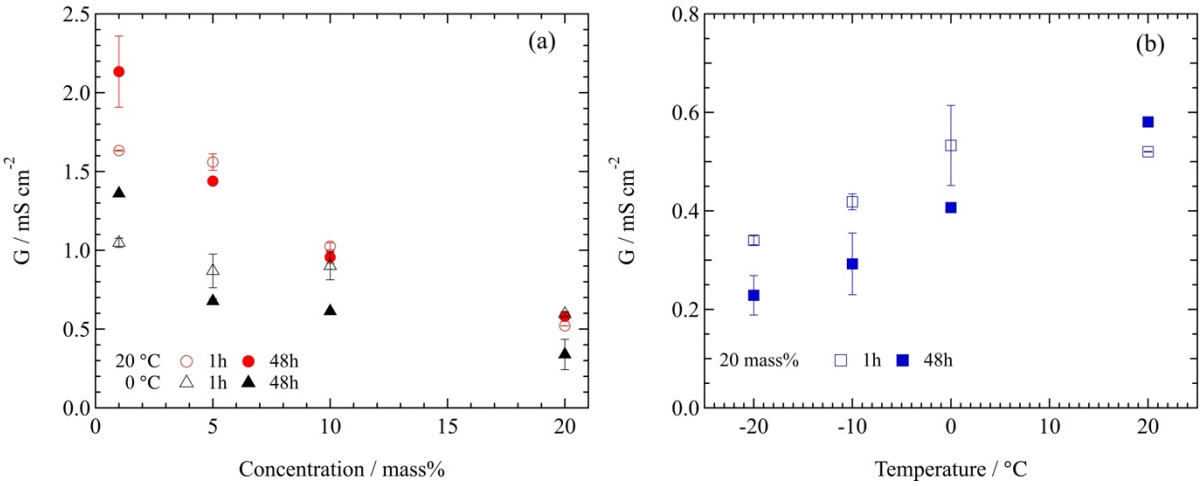


Fig. 7. Conductance, G, plotted as a function of the immersion time for carbons steel immersed in NaCl solutions with different concentrations or temperatures.

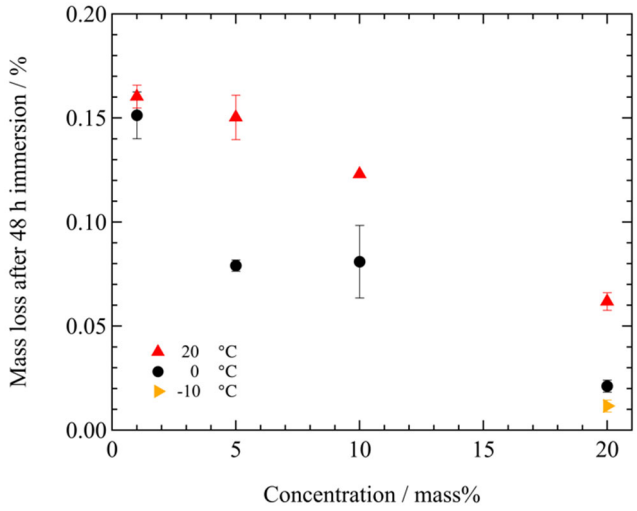


Fig. 8. Mass loss of specimens after 48 h immersion.

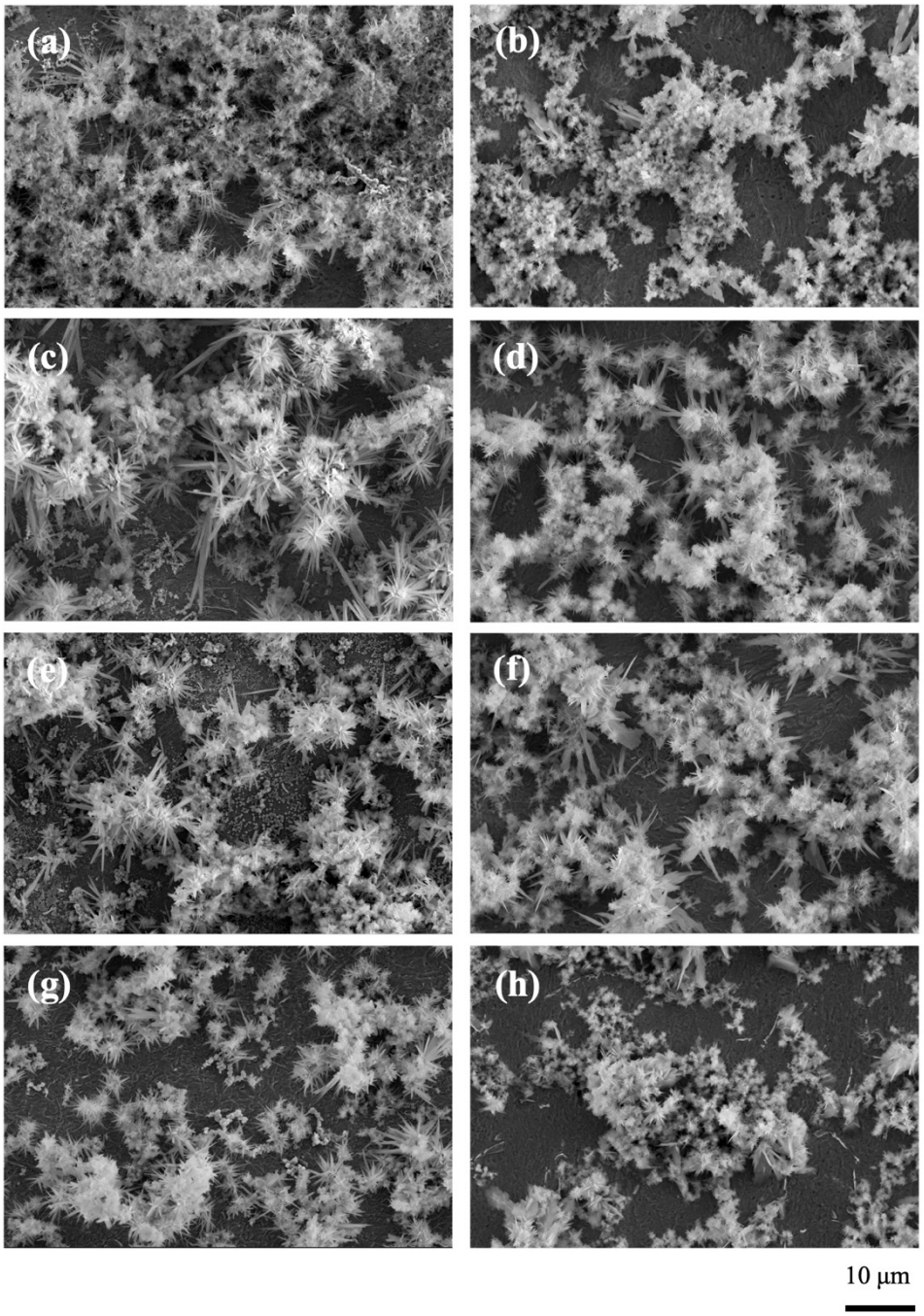


Fig. 9. Surface images of the corrosion product formed on the carbon steel at 20 ºC ((a)1 mass%, (c) 5 mass%, (c) 10 mass%, (g) 20 mass%), and 0 ºC ((b)1 mass%, (d) 5 mass%, (f) 10 mass%, (h) 20 mass%) after the immersion for 48 h.

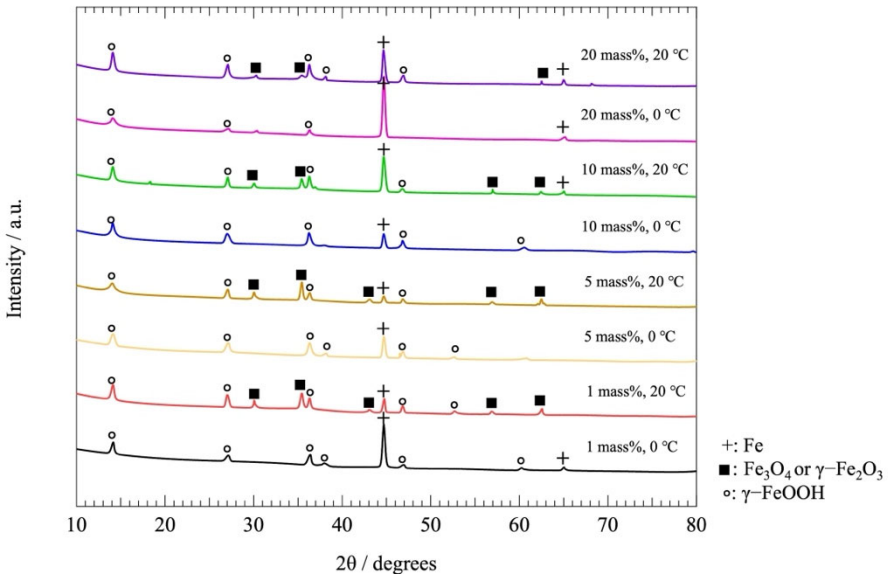


Fig. 10. XRD patterns of the corrosion products formed on specimens after immersion in the solutions for 48 h at 0 ºC and 20 ºC.

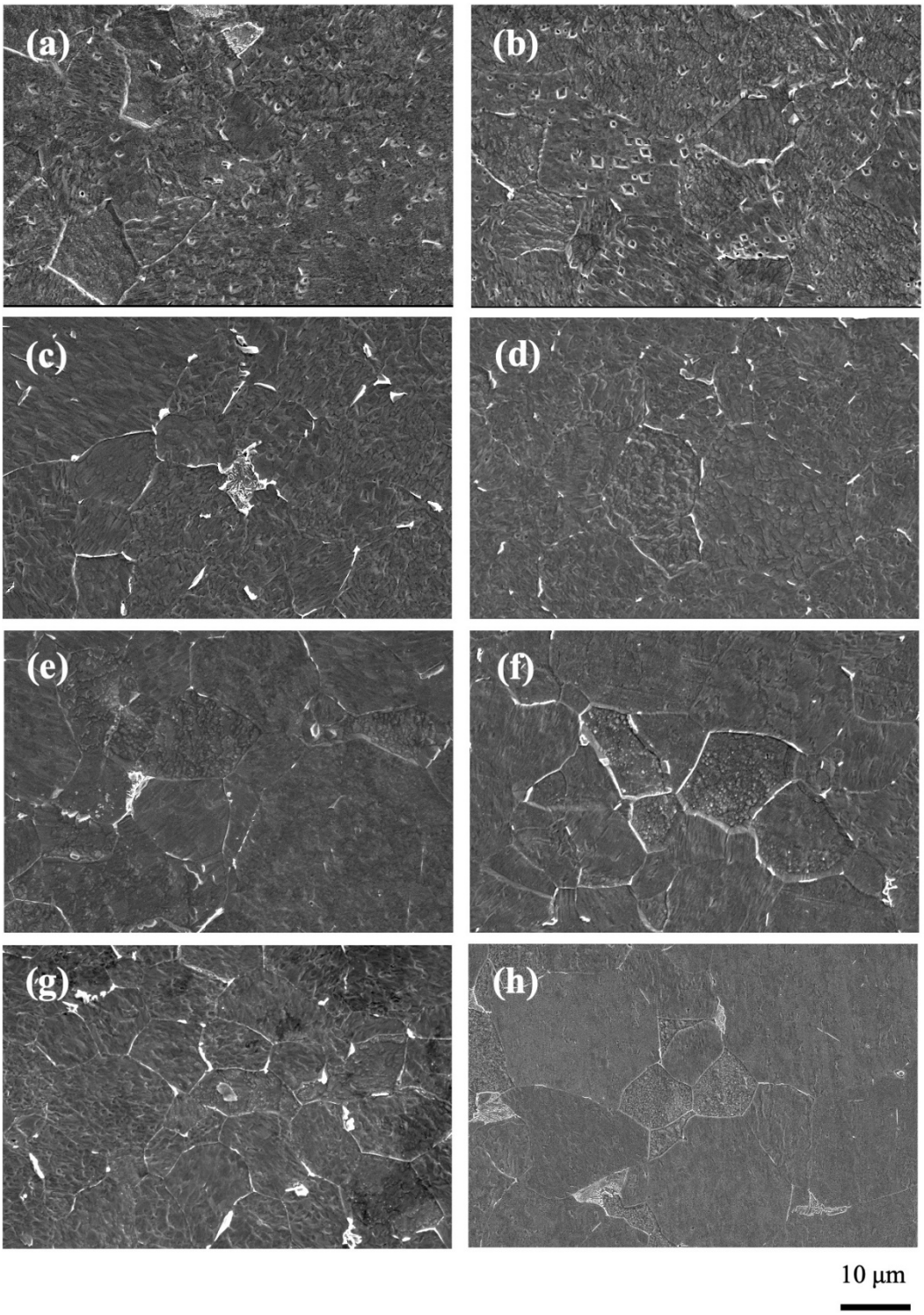


Fig. 11. Surface SEM images of specimen after immersion for 48 h in the solutions with different NaCl concentrations at 20 ºC((a)1 mass%, (c) 5 mass%, (c) 10 mass%, (g) 20 mass%) and 0 ºC ((b)1 mass%, (d) 5 mass%, (f) 10 mass%, (h) 20 mass%).

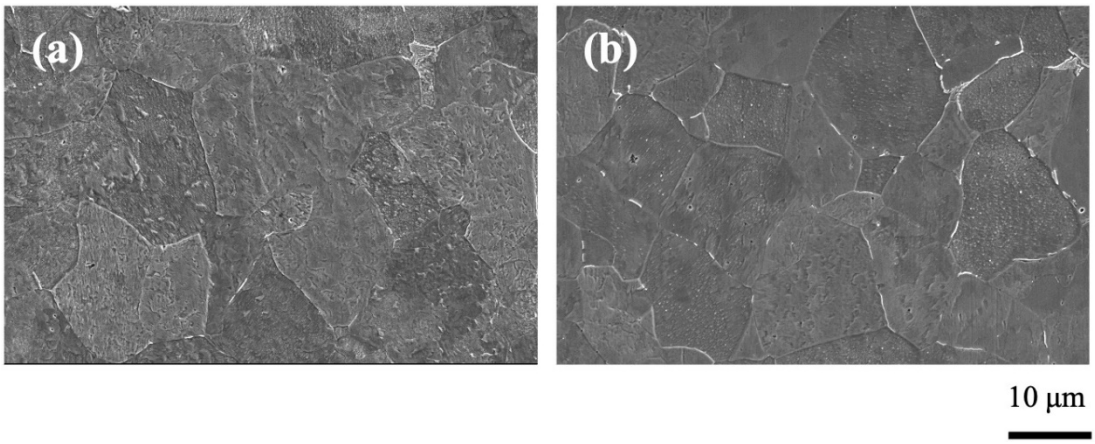


Fig. 12. Surface SEM images of specimen after immersion for 48 h in 20 mass% at (a) -10 ºC and (b) -20 ºC.

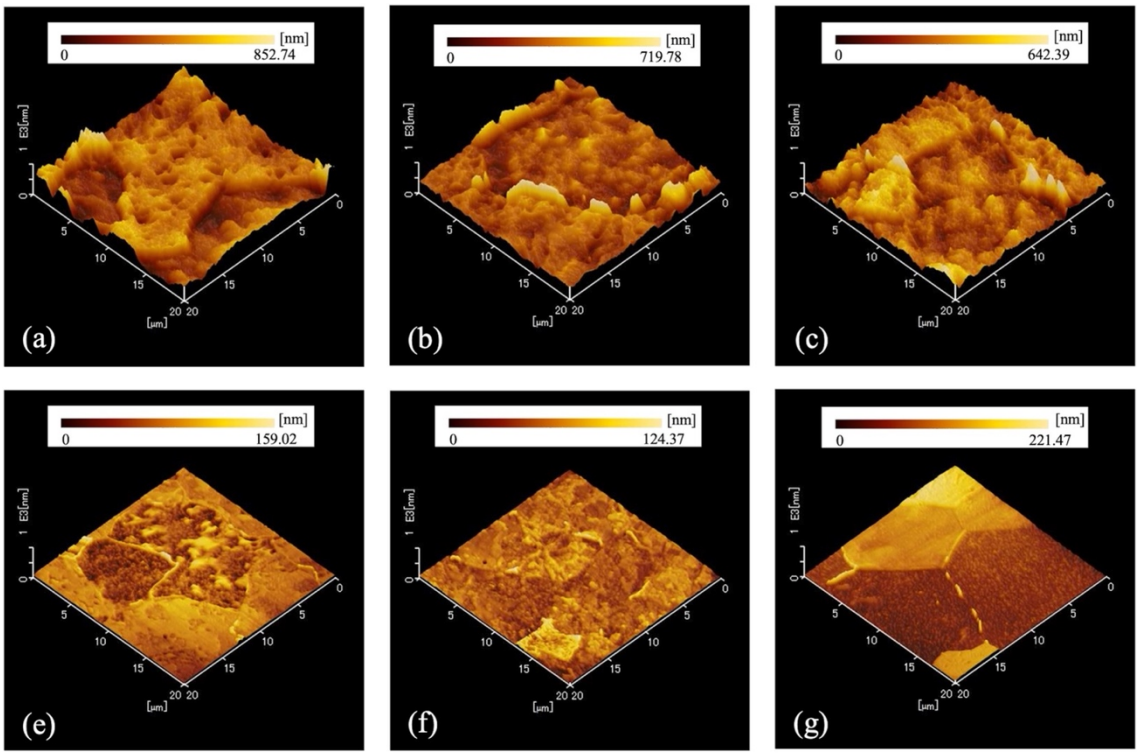


Fig. 13. AFM 3D images of carbon steel immersed in the solutions 48 h at 0 ºC in (a) 1 mass%; (b) 5 mass%; (c) 10 mass% and (d) 20 mass%; and at (f) -10 ºC and (g) -20 ºC in 20 mass%.

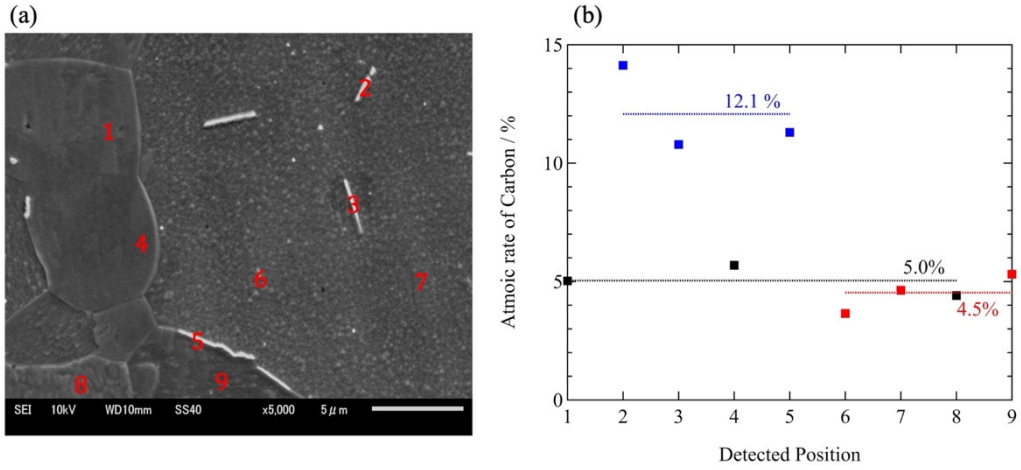


Fig. 14. SEM image (a) and EDS point analysis results (b) of specimen after 48 h in 20 mass% NaCl solution at -20 ºC.